



# Multifractal Characteristics of MIP-Based Pore Size Distribution of 3D-Printed Powder-Based Rocks: A Study of Post-Processing Effect

Lingyun Kong<sup>1</sup> · Mehdi Ostadhassan<sup>1</sup> · Bo Liu<sup>2</sup> · Chunxiao Li<sup>1,3</sup> · Kouqi Liu<sup>1</sup>

Received: 27 April 2018 / Accepted: 12 September 2018  
© Springer Nature B.V. 2018

## Abstract

3D printing technology offers an innovative approach to manufacture rock samples with controlled properties. However, in this process, pore structure is one of the major concerns when printing similar specimens to natural rocks. The purpose of this study was to lay out an optimal post-processing of 3D-printed samples that can facilitate replicating natural rocks with similar microstructure characteristics. In this study, four cylindrical rocks were manufactured without designed porosity by 3D printing using gypsum powder as the main component. Various types of infiltrants (Colorbond<sup>®</sup> and Surehold<sup>®</sup>) and coating conditions (SmoothOn<sup>®</sup> and WBAE<sup>®</sup>) were used after completing the printing process of binder jetting. Mercury injection porosimetry was then used to investigate their petrophysical properties including porosity and pore throat size distribution. Multifractal theory was applied to understand the heterogeneity of pore throat distribution within the 3D-printed samples on different pore size intervals. The results showed that 3D-printed rocks have a clustered and negative skewness of pore throat size distributions. The majority of pore sizes are micropores, while a small portion can be categorized under nanopore size category. Multifractal analysis results found a homogeneous distribution of micropores but a heterogeneous distribution of nanopores. Comparing four different samples, it was found that infiltrants could mainly affect the heterogeneous distribution of nanopores more than the micropores, whereas coating does not impact pore structure significantly. In comparison with pore multifractal characteristics of common types of natural rocks, 3D-printed rocks exhibited a higher heterogeneity of pore size distribution.

**Keywords** 3D-printed rock · Post-processing · Multifractal analysis · Pore throat size distribution

---

✉ Lingyun Kong  
lingyun.kong@und.edu

✉ Mehdi Ostadhassan  
mehdi.ostadhassan@enr.und.edu

Extended author information available on the last page of the article

## 1 Introduction

Reconstituted rock proxies are efficient substitutes for characterizing petrophysical, geomechanical, and transport properties of natural rocks in the laboratory. In a conventional approach, various rock properties are investigated by using inch-size core plugs that are retrieved from subsurface (Wang 2002a, b; Ling et al. 2016; Zhao et al. 2017a; Wang et al. 2018a, b). However, core plugs can be limited, costly to access and hard to obtain. Furthermore, most of these experiments on the samples are destructive and once the study is completed they cannot be used for further analysis. In addition, when attempting to develop a model, an adequate number of samples are required. Adding the variability that exist in different properties in each sample, it has led researchers to explore additional experimental methods with various techniques in geoscience and engineering (Wang et al. 2017; Xiong et al. 2017; Li et al. 2018a, b; Khatibi et al. 2018; Zhang et al. 2018; Ostadhassan et al. 2018; Chen et al. 2018; Gong et al. 2018).

Researchers have attempted to manufacture proxies in terms of mineralogy, texture and structure, by mimicking the sedimentation, diagenesis as well as compaction processes that were occurred in paleoenvironment (Squelch 2018). Tien and Tsao (2000) prepared an artificial transversely isotropic rock through high-pressure compaction of mixtures of cement, sand, microsilica and kaolinite to measure geomechanical performance of samples under uniaxial and triaxial testing. Saidi et al. (2005) prepared a poorly consolidated granular rock by mixing various proportions of fine and coarse sand, cement and water, which were tested under uniaxial compression experiments to investigate the impact of cement content. Tillotson et al. (2012) manufactured two synthetic sandstones by enabling silica cementation of quartz sand grains and validated the relationship between fracture density and shear-wave splitting. Ding et al. (2014) constructed new synthetic rocks with controlled fractures and analyzed seismic anisotropy as a function of fracture density and fluids.

Recent advances in additive manufacturing, known as 3D printing, offers the potential to carry out experiments to better understand different types of porous natural rocks by controlling parameters in a repeatable manner. Ishutov et al. (2015) presented a workflow for transferring digital rock models to tangible samples by combining X-ray computed microtomography data, digital pore network modeling as well as 3D printing. Head and Vanorio (2016) generated 3D-printed models by micro-CT scanned images of carbonate reservoir rocks to study the impact of rock microstructures on transport properties. Fereshtenejad and Song (2016) evaluated the effect of printing direction, layer thickness and binder saturation on geomechanical properties of the powder-based samples and proposed methodology to improve the performance of 3D-printed rock models. Jiang et al. (2016) conducted tentative compressive and shearing experiments on 3D-printed rocks made up of two types of materials, sand-powder based and polylactic acid based. Kong, et al. (2017) performed uniaxial compression experiments and studied the effect of specimen size on 3D-printed rocks in gypsum powder. Tian and Han (2017) used selective laser sintering and powder-binder methods to print synthetic rocks and conducted uniaxial compression and splitting tensile tests. Vogler et al. (2017) compared tensile failure properties and surface roughness of natural sandstones and 3D-printed samples. Ishutov et al. (2017) produced 3D-printed porous proxies of Fontainebleau sandstone at different magnifications of pore network, aiming to investigate transport properties of porous media at variable scales. Suzuki et al. (2017) created samples with different fracture networks and distributions to validate classic permeability models. Kong et al. (2018a, b) proposed a comprehensive approach to obtain the accurate porosity value and pore size distribution of 3D-printed rocks made from gypsum powder

without designed pore network. As above, the previous studies improved the understanding of microstructure, petrophysical and geomechanical properties of rock analogues 3D-printed in gypsum powder. Despite recent efforts to employ additive manufacturing in geoscience research, the application of 3D printing technology in this field is still in the preliminary phase. Some potential future directions for the application of 3D printing can be: validating numerical simulations and complementing existing laboratory experiments, generating rescaled representations of surface or subsurface morphologies and relief on planetary bodies, etc. (Ishutov et al. 2018).

Primkulov et al. (2017) and Hodder et al. (2018) elaborated that the post-processing treatment, specifically the curing of the samples, plays an essential role in forming a rock-like behavior in terms of microstructure and geomechanical properties. However, it remains vague how the post-processing (infiltration and coating) impacts the microstructure of 3D-printed rocks, which requires further attention. Therefore, this study compared the microstructure of four gypsum-based analogues post-processed with various types of infiltrants and coatings. In this regard, mercury injection porosimetry (MIP) and gas permeameter were conducted on these samples to obtain the pore structure and petrophysical properties. In the next step, the effect of post-processing was evaluated on the heterogeneity of the microstructures by analyzing multifractal dimensions. Ultimately, the results were compared to suggest the best infiltrant and coating type that can provide the most homogenous and heterogeneous microstructures within the samples for future applications that may resemble a homogeneous natural rock.

## 2 Methodology

### 2.1 Description of Samples

3D printing proxies followed a standard procedure described in Kong et al. (2017). Digital rock models were created in a computer-aided design and drafting (CAD) software. Then the printer read STL files as input to start the printing process. Four cylindrical samples were manufactured by the binder jetting printing method, 3D systems Projet 660 printer, using the same material as Visijet PXL core and binder. The printing layer thickness was 0.004 inches or 0.1 mm. The chemical composition of the binder was 2-pyrrolidone with 1% concentration. Based on the results by Fereshtenejad and Song (2016), the direction of printing and how each layer is deposited will cause elastic anisotropy in cylindrical samples. However, material properties in all directions perpendicular to the vertical axis of symmetry (the printed layers) are mostly similar, indicating vertical transverse isotropic (VTI) behavior for 3D-printed rocks by binder jetting method. Considering sedimentary rocks, for instance shales, VTI model has been commonly developed and applied (Ramamurthy 1993; Nasseri et al. 2003; Ostadhassan et al. 2012; Brady and Brown 2013), which was also found in the microstructure study of powder-based 3D-printed rocks (Kong et al. 2018b). Therefore, in this study, it was decided to print the samples from bottom to the top horizontally to form a cylinder to represent a VTI model.

During the infiltration process, the infiltrant would penetrate into the voids due to the capillary forces in the smaller pores, 2–7 mm deep into the sample from surface (Kunchala and Kappagantula 2018). The coating is expected to be on the surface, generating a shallower penetration but higher strength in the samples (Taha et al. 2005; Stumpf et al. 2018). This addition remarkably improved the bulk modulus and strength of artificial rocks (Choi et al.

**Table 1** Chemical components and concentrations of four 3D printed rock samples

| Sample ID | Infiltrant brand    | Chemical name   | Concentration (%) |
|-----------|---------------------|---|-------------------|
| 1         | Colorbond           | Methoxyethyl cyanoacrylate  | 80–100            |
| 2         | Surehold            | Methoxyethyl cyanoacrylate  | 70–100            |
| 3         | Smooth on (coating) | Oxirane, 2,2'-((1-methylethylidene)bis(4,1-phenyleneoxymethylene))bis-, homopolymer | 100               |
| 4         | WBAE (coating)      | Diethanolamine + Methoxypropanol  | 100               |

2017; Guo et al. 2017). To study the effects of post-processing steps (infiltration and coating) on the pore structures, samples with different infiltrants and coatings were manufactured in this study. Samples 1 and 2 were infiltrated by Colorbond<sup>®</sup> and Surehold<sup>®</sup>, respectively, while samples 3 and 4 were coated using SmoothOn<sup>®</sup> and WBAE<sup>®</sup>. Detailed chemical components and concentrations for each sample are listed in Table 1, in which Colorbond and Surehold have the same chemical composition but different concentrations.

## 2.2 Mercury Injection Porosimetry (MIP) and Gas Permeability Measurement

Mercury injection porosimetry (MIP) is a commonly used method for evaluating pore characteristics such as pore structure, capillary pressure, and pore size distribution of geomaterials (Giesche 2006; Malik et al. 2016). PoreMaster-60 manufactured by Quantachrome instruments was used in this study to conduct the MIP experiments on all four samples. A pressurized chamber pushed the mercury into the pore throats, in which the pressure increased as mercury intruded first larger pores followed by the smaller ones. The Washburn equation was applied to relate the injection pressure to the distribution of pore throat size (Webb 2001). Pulse Decay Permeameter-PDP-200 which is suitable for the low-permeability rock with the measurement range of 0.00001–10 mD was employed to measure the Klinkenberg permeability using nitrogen under confining pressure of 1500 Psi. Different from the steady-state method, this system saturates the samples to a set pore pressure and then generates a differential pressure pulse through the cylinder (Knabe et al. 2011).

## 2.3 Multifractal Theory

Fractals are self-similar objects that occur identically on all scales of magnifications (Mandelbrot 1983; Lopes and Betrouni 2009). It has been proved that pore network of natural rocks has a fractal nature based on previous extensive studies (Katz and Thompson 1985; Hansen and Skjeltorp 1988; Costa 2006; Dullien 2012; Clarkson et al. 2013; Wang et al. 2016). Fractal geometry has been used to imply the spatial heterogeneities over pore spaces especially in sedimentary rocks (Wong et al. 1986). In this regard, multifractal analysis has the advantage to understand more sophisticated distributions of void spaces in rocks compared to single fractal dimension as it requires a series of generalized fractal dimensions (Bird et al. 2006). Fractal dimension and multifractal spectra are also found to correlate well with basic rock properties, for instance measured permeability (Li et al. 2016a) and porosity (Liu

et al. 2017). Therefore, estimating fractal and multifractal characteristics of synthetic rocks that are created by 3D printing without porosity could be one of the main attributes of their similarity to natural rocks. Experimental methods that can provide continuous information about fractal dimensions and multifractal spectra of pore structures include mercury intrusion porosimetry (MIP), nuclear magnetic resonance spectroscopy (NMR), small-angle neutron scattering (SANS), etc. (Daigle et al. 2014; Zhou et al. 2016; Zhao et al. 2017b). Hence, in this study fractal geometry in 3D-printed rocks was discussed based on MIP experiments for pore size distribution (PSD) to understand self-similarity of pores and as a measure for proximity to a natural rock.

Multifractal analysis could be implemented on PSDs by one-dimensional mercury injection of the pore size interval (Vázquez et al. 2008). First, a series of boxes or subintervals of equal length  $\varepsilon$  in the interval  $l = [a, b]$  were set, which could be partitioned into a number of boxes  $N(\varepsilon) = 2^k$  with the box size  $\varepsilon = L \times 2^{-k}$  in  $k$  stages ( $k = 0, 1, 2, 3 \dots$ ), where  $L$  is the whole interval length.

Based on both the resolution and result of MIP experiments in this study, the pore size interval would vary from 0.003 to 18  $\mu\text{m}$ , which could be divided into 20 subintervals of a single length of 0.9  $\mu\text{m}$ ,  $l_i = [a_i, a_{i+1}]$  ( $i = 1, 2, 3 \dots, 20; a_{i+1} - a_i = 0.9\mu\text{m}$ ). Considering box counting algorithm, in each subinterval (box), the Hg saturation fraction,  $V_i$ , was measured, the sum of which equals 1. Prior to the calculation of box counting, the pore size interval  $l$  should be normalized into  $[0,1]$  so that is comparable among all samples. Considering each box that should have a valid value of pore volume, the number of box or subintervals is set as  $N(\varepsilon) = 2^k$  with maximum  $k = 4$ . From  $k = 0$  to 4, each subinterval could be measured by the corresponding Hg saturation fraction as  $p_i(\varepsilon)$ .

Partition function is used to analyze the relationship between probability density distribution of  $p_i$  with Hg saturation fraction, which should be previewed whether the sample is suitable to multifractal analysis. This equation is given below (Vázquez et al. 2008):

$$\chi(q, \varepsilon) = \sum_{i=1}^{N(\varepsilon)} p_i^q(\varepsilon) \tag{1}$$

where the moment order  $q$  is a real number, the range is from  $-\infty$  to  $+\infty$ , which could represent different segments of pore throat size distributions (Li et al. 2015). For  $q \ll 1$ , the value of  $\chi(q, \varepsilon)$  is dominated by small value of  $p_i(\varepsilon)$ , while for  $q \gg 1$ , it is mainly controlled by large value of  $p_i(\varepsilon)$ . As it is explained by Grassberger and Procaccia (1983), a series of generalized dimensions,  $D_q$ , can be used to represent the porosity distribution via the following equation:

$$D_q = \lim_{\varepsilon \rightarrow 0} \frac{1}{q-1} \frac{\log[\chi(q, \varepsilon)]}{\log(\varepsilon)} = \lim_{\varepsilon \rightarrow 0} \frac{1}{q-1} \frac{\log\left[\sum_{i=1}^{N(\varepsilon)} p_i^q(\varepsilon)\right]}{\log(\varepsilon)} \tag{2}$$

For  $q = 1$ , Eq. (2) should be determined by L'Hôpital rule as (Feder 2013):

$$D_1 = \lim_{\varepsilon \rightarrow 0} \frac{\sum_{i=1}^{N(\varepsilon)} p_i(\varepsilon) \log[p_i(\varepsilon)]}{\log(\varepsilon)} \tag{3}$$

The  $D_q$  spectrum can be calculated based on the above relationship between  $q$  and  $D_q$ , in which  $D_0, D_1, D_2$  are capacity dimension, information dimension and correlation dimension, respectively. The correlation dimension can also be expressed as (Riedi et al. 1999)

$$D_2 = 2H - 1 \tag{4}$$

where  $H$  is Hurst exponent and varies from 0.5 to 1, typically relevant to long-range spatial variation and its positive autocorrelation. Based on the theory, if the fractal is statistically self-similar or homogeneous, the  $D_q$  should be exactly equality. While for multifractal distribution, the result demonstrates a decreasing function with a sigmoidal shape on the spectrum, in which  $D_0 > D_1 > D_2$  (Caniego et al. 2003). In summary,  $D_q$  spectrum is used to characterize the heterogeneity or complexity of pore structures.

## 3 Results

### 3.1 Porosity and Permeability

Porosity, permeability as well as other basic physical parameters of four samples were measured and compared (Table 2). Unlike natural rocks, artificial rocks made by 3D printing, intact samples specifically, do not contain micro-fractures (Jiang et al. 2016; Kong et al. 2018b). The porosity of sample 1 compared to sample 2 expressed a significant difference although same gypsum powder and binder were used in the printing process. It can be interpreted as the impact of infiltrant on the petrophysical properties of 3D-printed rocks. Infiltrant of higher concentration, which resulted in penetrating slower into the pore network, created larger pore space volume (Table 1). The grain density of sample 1 was found to be the largest among all four samples, as a result of higher concentration and density of infiltrant. Samples 3 and 4 were measured to have the least porosity due to the coating on the exterior of the synthetic rocks, which might hinder the mercury injection during MIP experiments. Gas (Nitrogen) permeability experiments were carried out under confining pressure of 1500 Psi which exhibited similar trends with the porosity values, representing samples with low permeability (Schön 2015).

### 3.2 Pore Structure Characterization

MIP experiments can provide insight into pore throat structure and size distributions in porous media from 3.6 nm to 950  $\mu\text{m}$  in diameter (Shen et al. 2016). Based on the morphological analysis of capillary pressure curves by Wardlaw and Taylor (1976), it is known that a clustered distribution of pore throat sizes results in a horizontal segment of the curves while an inclined curve refers to a uniform distribution for more pore sizes. Additionally, negative skewness, which results in the pressure–saturation curve toward lower-left corner of the plot, indicates the concentration of larger pores in pore size distribution (PSD) (Li et al. 2016b). Oppositely, positive skewness makes the curve to get closer to the upper-right corner (Li et al. 2016b). From the results of MIP experiments, all the capillary pressure curves demonstrate a clear horizontal segment of approximately 55% of mercury saturation, which is an indication of a significant cluster of pore throats size in 3D-printed samples (Fig. 1). Samples 1 and 4 exhibited additional 10% for mercury saturation in the horizontal segment than samples 2 and 3. All pressure curves almost appear closer to the lower-left region of the plot specifically on the logarithmic scale of y-axis, which reflects the negative skewness of pore size distribution that could be validated by further analysis. 3D-printed rocks have a dominant pore size and negative skewness of pore throat distributions with different infiltrants to impact the pore characteristic.

The entry pressure is the point on the capillary pressure curve where the mercury first intrude into the sample pores, denoting the largest pore size that mercury could have accessed

**Table 2** Summary table of basic parameters of four 3D printed gypsum-powder-based samples

| Sample ID | Length (cm) | Diam. (cm) | Caliper bulk vol (cc) | Dry weight (gm) | Grain volume (cc) | Grain density (gm/cc) | Pore volume (cc) | Porosity (%) | Permeability (mD) |
|-----------|-------------|------------|-----------------------|-----------------|-------------------|-----------------------|------------------|--------------|-------------------|
| 1         | 3.852       | 2.55       | 19.672                | 30.661          | 15.501            | 1.978                 | 4.17             | 21.198       | 0.006589          |
| 2         | 3.849       | 2.553      | 19.703                | 30.857          | 19.298            | 1.599                 | 0.404            | 2.05         | 0.001882          |
| 3         | 3.797       | 2.56       | 19.544                | 30.845          | 19.514            | 1.581                 | 0.03             | 0.153        | 0.000005          |
| 4         | 3.821       | 2.556      | 19.606                | 30.341          | 19.480            | 1.558                 | 0.126            | 0.643        | 0.000074          |

**Fig. 1** Capillary pressure curves of four 3D printed samples

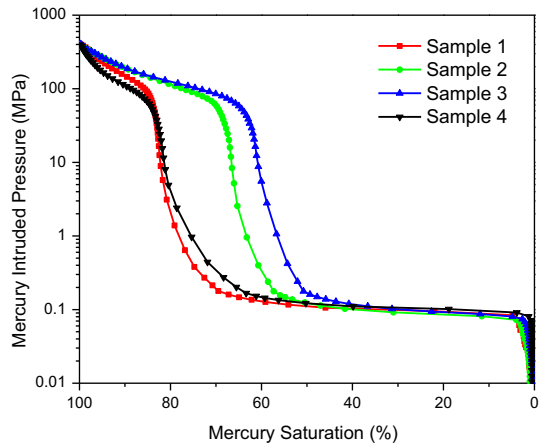
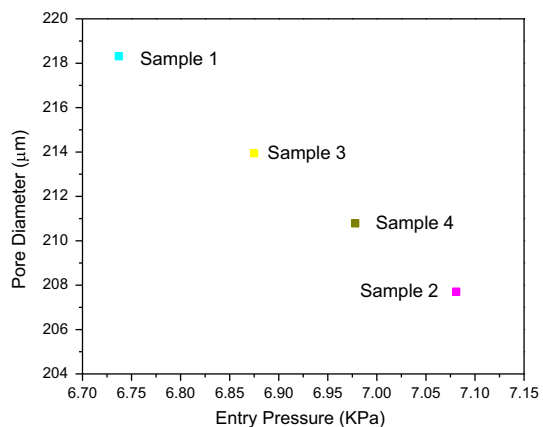


**Fig. 2** Entry pressure and corresponding pore diameters of four samples



(Nabawy et al. 2009). Four samples have the entry pressure varying from 6.73 to 7.08 kPa, in which sample 1 has the greatest corresponding pore diameter of 218  $\mu\text{m}$  among four samples (Fig. 2). The calculated pore throat diameter distributions of four samples were compared (Figs. 3, 4). Negative skewness was observed in all samples, confirming the above capillary pressure curves. According to pore size classification by Loucks et al. (2012), the majority of pore sizes lie between 10 to 20  $\mu\text{m}$ , which belongs to the micropore category. A small portion of pores was measured in the 10–20 nm interval, representing nanopore size category.

The relationship between mercury saturation divided by capillary pressure and mercury saturation was introduced to identify the apex point which can explain the transition from well-connected pores to poorly connected ones (Pittman 1992; Nabawy et al. 2009). The capillary pressure corresponding to the apex point is known as surface entry pressure, denoted by  $P_{c_{\text{apex}}}$ , which is related to transport properties of the porous media, such as permeability, based on experiments that were conducted on natural rocks (Lai and Wang 2015). Therefore, it would be beneficial to determine the surface entry pressure to compare this pore connectivity parameter with other rock types.  $P_{c_{\text{apex}}}$  of samples 1–4 are 0.127, 0.113, 0.119, 0.134 MPa, respectively (Fig. 5).

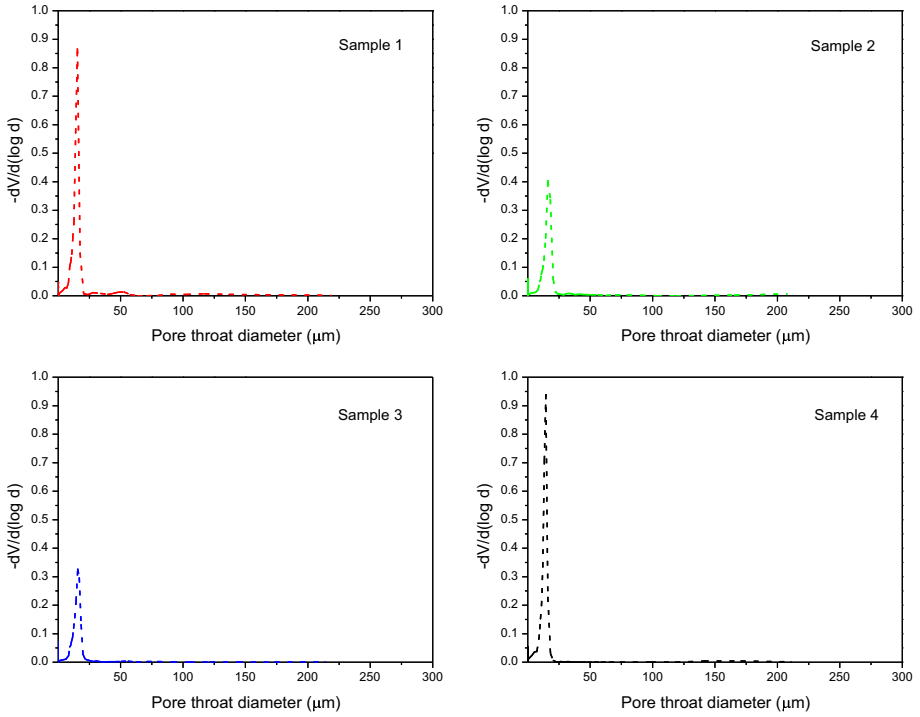


**Fig. 3** Pore throat size distribution based on MICP measurements. (Note X-axis is normal scale)

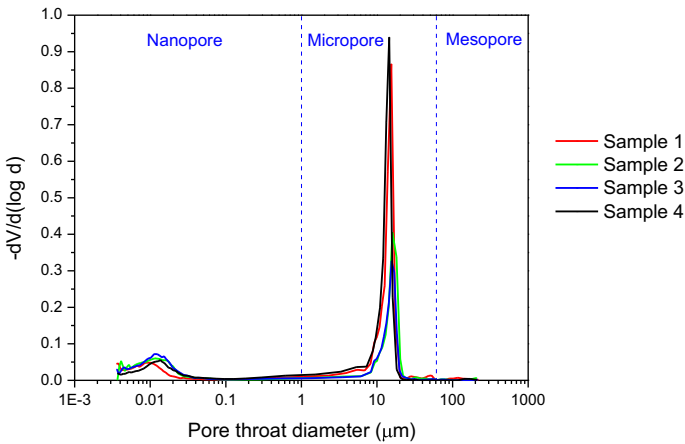


**Fig. 4** Distribution curves of pore throat diameter of four samples. (Note X-axis is logarithmic scale)

### 3.3 Fractal Analysis

Prior to investigating the fractal characteristics of 3D-printed rocks, one should examine whether the pore throat size distribution in this synthetic porous media has the feature of multifractal distribution (Muller 1996). If a power law or linear function is applied to the

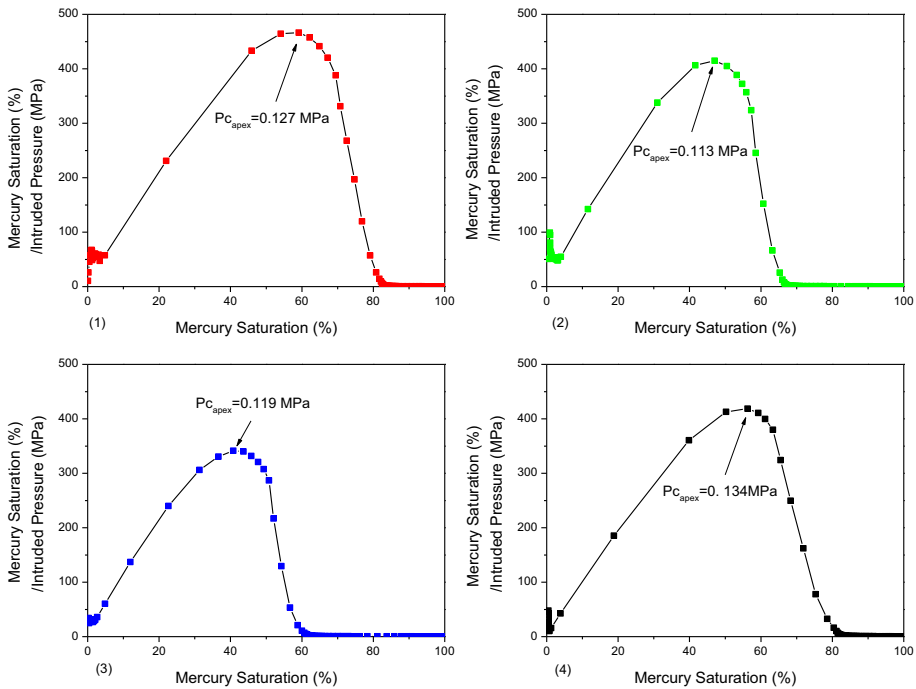


**Fig. 5** Plots of mercury saturation/intruded pressure (MPa) versus mercury saturation (%).  $P_{c_{apex}}$  are identified for sample 1–4, which are 0.127 MPa, 0.113 MPa, 0.119 MPa, 0.134 MPa, respectively

plot of partition functions and box sizes in terms of each moment of  $q$  varying from  $-10$  to  $10$ , then pore throat distribution has multifractal characteristics (Muller 1996). Through the multifractal analysis of MIP experiments, the linear fitted curves match the data of each moment order of  $q$ , with the coefficients of correlation,  $R^2$  all above 0.9 (Figs. 6, 7, 8, 9). To compare four samples, average correlation coefficients,  $R^2$ , were calculated as 0.96383, 0.991, 0.98906, 0.96615, respectively, which are strong evidence of multifractal characteristics of pore throat size distribution of 3D-printed gypsum-powder rocks.

Based on Eqs. (2) and (3), generalized dimensions,  $D_q$  or  $D(q)$ , were calculated for each sample and the spectra were compared (Fig. 10). It is evident that all  $D(q)$  spectra follow a decreasing trend monotonically as  $q$  varies from  $-10$  to  $10$  with a sigmoidal shape. Three key dimensions in this case also follow the order of  $D_0 > D_1 > D_2$ , which confirms the conclusion from the log–log plots of partition function that pore throat structures in the 3D-printed samples have the multifractal properties (Figs. 6, 7, 8, 9). Additional inner variations were also interpreted from the spectra (Table 3), in which the analyzed parameters include information dimension  $D_1$ , Hurst exponent ( $H$ ) and the spectrum width  $D_{-10} - D_{10}$ . The wider the  $D(q)$  spectrum is, the higher the heterogeneity or complexity of pore structures in the porous media should become (Vázquez et al. 2008). Sample 1 was found to have the widest distribution of  $D(q)$  spectrum, 1.7116 of  $D_{-10} - D_{10}$ , exhibiting the highest heterogeneity of pore throat size distribution. Sample 3 was found to have the narrowest distribution of  $D(q)$  spectrum, 0.9984 of  $D_{-10} - D_{10}$ , indicating the lowest inhomogeneity of pore throat size distribution.

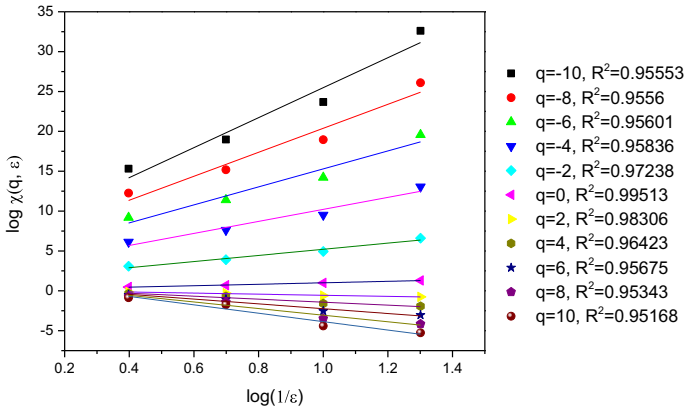


**Fig. 6** Log plots of the partition function versus box size based on PSD of sample 1. Note that different colors denote different,  $q$ , followed by coefficients of determination,  $R^2$

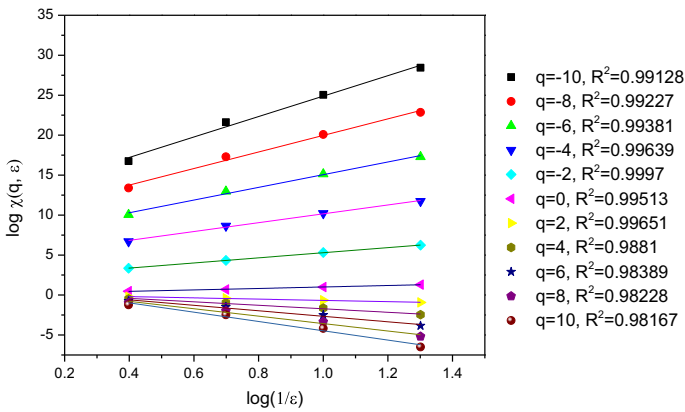
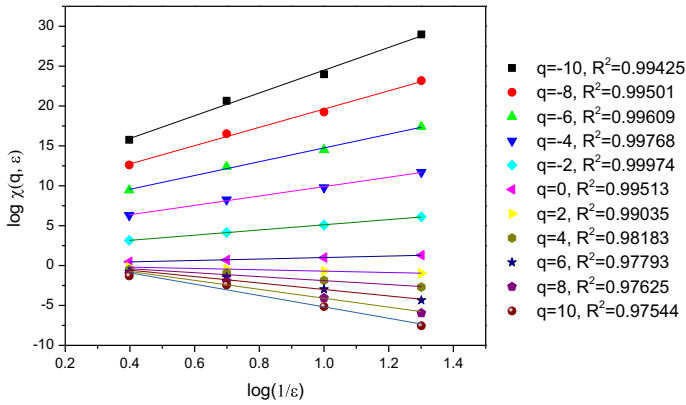


**Fig. 7** Log plots of the partition function versus box size based on PSD of sample 2. Note that different colors denote different,  $q$ , followed by coefficients of determination,  $R^2$

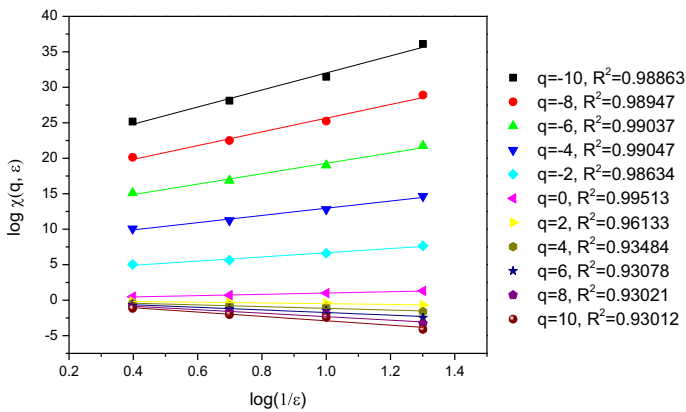
**Table 3** Multifractal parameters obtained from generalized dimension spectrum of four samples

| Sample ID | $D_0$  | $D_1$   | $H$     | $D_{10}$ | $D_{-10}$ | $D_{-10}-D_{10}$ | $D_0-D_{10}$ | $D_{-10}-D_0$ |
|-----------|--------|---------|---------|----------|-----------|------------------|--------------|---------------|
| 1         | 0.9905 | 0.8312  | 0.83595 | 0.5706   | 2.2822    | 1.7116           | 0.4199       | 1.2917        |
| 2         | 1.0332 | 0.83535 | 0.8803  | 0.6241   | 1.702     | 1.0779           | 0.4091       | 0.6688        |
| 3         | 1.0332 | 0.88606 | 0.91975 | 0.7878   | 1.7862    | 0.9984           | 0.2454       | 0.753         |
| 4         | 1.0332 | 0.81857 | 0.8772  | 0.553    | 2.2229    | 1.6699           | 0.4802       | 1.1897        |

It has been documented that variation of spectrum width for different samples is the result of many different factors in natural rocks (Li et al. 2015). For instance in coal, the variation of multifractal characteristics is relevant to maceral type, carbon and ash content, coal rank and even tectonic deformations (Hou et al. 2012; Giffin et al. 2013) which reflects the complexity of components and processes that the rock has gone through over time.

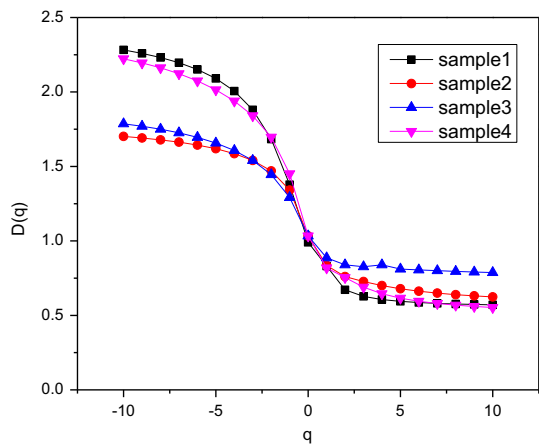


**Fig. 8** Log plots of the partition function versus box size based on PSD of sample 3. Note that different colors denote different,  $q$ , followed by coefficients of determination,  $R^2$



**Fig. 9** Log plots of the partition function versus box size based on PSD of sample 4. Note that different colors denote different,  $q$ , followed by coefficients of determination,  $R^2$

**Fig. 10** Generalized dimension  $D(q)$  versus moment order  $q$  from  $q = -10$  to  $q = 10$  based on the fractal analysis of PSD obtained from MICP experiments



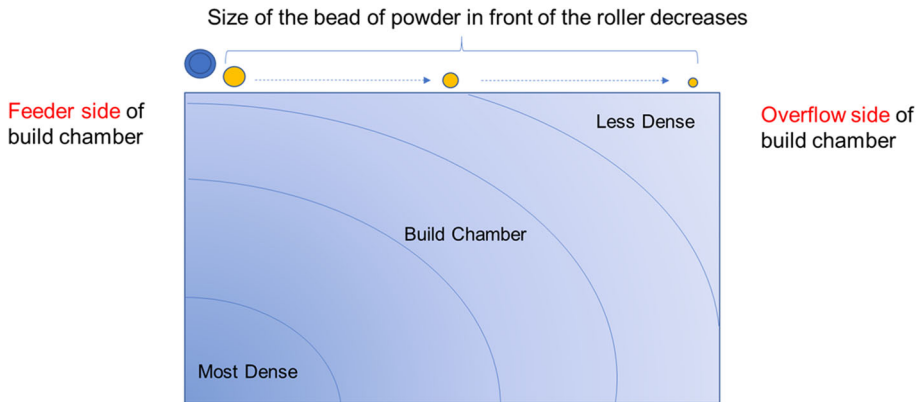


**Fig. 11** Heterogeneity of material density distribution caused by powder bead size decreasing

However, the 3D-printed rock samples are very simple compared to natural rocks in both components and the process of formation. Hence, there should be only two main factors that can affect the heterogeneity of pore throat size distribution (presuming known printing system and material). The first is the “squash effect” which is caused by the process in which the sample orientation is placed in the build chamber of a printing device (Oropallo and Piegler 2016) (Fig. 11). Given the chamber having two sides, feeder side and overflow side, the size of powder beads in the front of the roller decreases from the feeder side to the overflow side. Therefore, the density of printing should have the same trend similar to the size of powder beads. Nevertheless, in samples with regular shapes like a cylinder, one should not expect any difference if the sample is placed upright. Another factor is the infiltration after the printing process, which cannot penetrate completely into inner parts of the sample (Kunchala and Kappagantula 2018).

Based on the comparison of the inner variation of spectra, the segments of  $q < 0$  show typical sigmoidal shape, whereas the segments of  $q > 0$  illustrate quasi-linear behavior, especially for  $2 < q < 10$  (Fig. 10). The best fitting curve can also be verified by the widths of the left and right lobes of  $D(q)$  spectra. The values of  $D_{-10} - D_{10}$  are larger than the values of  $D_0 - D_{10}$  for all samples, which could be interpreted by the dominance of larger and smaller pore throat sizes, respectively (Table 3). The spectrum variation for  $q > 0$  corresponds to the seepage-pores (diameter larger than 100 nm), and the variation for  $q < 0$  results from adsorption-pores (diameter smaller than 100 nm) (Caniego et al. 2003), shown in Fig. 4. The boundary between nanopores and micropores is 1000 nm (1  $\mu\text{m}$ ). However, since the pore throat size distribution concentrates on two clusters, one around 10 nm (0.01  $\mu\text{m}$ ) and the other one around 10  $\mu\text{m}$  (Fig. 4), both pairs of categories were considered to be equivalent in this study.

Sigmoidal shape of the curve represents a heterogeneous distribution of pore throat sizes while quasi-linear shape shows a homogeneous distribution of pore throat sizes. Therefore, 3D-printed rocks display a homogeneous structure of seepage-pores distribution but a heterogeneous structure of adsorption-pores. Sample 1 with higher concentration of infiltrant showed a larger spectrum width of  $D_{-10} - D_{10}$ , left-side width of  $D_{-10} - D_0$  and the right-side width of  $D_0 - D_{10}$  than sample 2 with less concentration of infiltrant. Comparing un-coated samples 1 and 2 with coated sample 3 and 4, infiltration has more impact than coating on the heterogeneous distribution of pore throat size in 3D-printed rocks. Additionally, the dif-

ference between sample 1 and 2 with respect to the left lobe width was calculated to be 0.6229, whereas the difference between these two samples for the right-side width was found 0.0108. These results verify that infiltrants mainly affect the heterogeneous distribution of adsorption-pores (or nanopores) based on the classification by Loucks et al. (2012) than seepage-pores (or micropores), which is compatible with the results directly obtained from pore throat size distribution in Sect. 3.2.

The capacity dimension  $D_0$ , expressed as  $\lim_{\varepsilon \rightarrow 0} \frac{\log \chi(\varepsilon)}{\log(\varepsilon)}$ , should correspond to the Euclidean dimension of PSD since partition function equals to the total number of boxes, no matter the box size (Li 2002). From Table 3,  $D_0$  value of four samples are very close to 1, which is in line with the conclusion of previous studies (Vázquez et al. 2008; Martínez et al. 2010; Li et al. 2015).  $D_1$  is the dimension that explains the concentration degree of the porosity spread across the pore size interval (Liu et al. 2018). When  $D_1$  is closer to  $D_0$ , a more uniform distribution of pore size distributions is expected across the pore size intervals (Liu et al. 2018). Thus, sample 3 has the smallest  $D_1 - D_0$ , demonstrating the most evenly distribution of pore throat size intervals for this sample compared to others (Table 3), while sample 4 has the smallest  $D_1$ , or the largest  $D_1 - D_0$  value representing the least uniform distribution of pore throat intervals. These findings are in agreement with the pore throat size distributions results that are observed in Fig. 4.  $H$ , known as Hurst exponent, which originally characterizes the memory or long-range dependency of the stochastic process in physics, can show the autocorrelation of pore throat size distributions (Martínez et al. 2010). The  $H$  of four samples is all close to 1 which means a strong autocorrelation in pore variations for various pore size intervals (Table 3).

In this study multifractal analysis was utilized, by evaluating various parameters, to get a better insight into the heterogeneity of pore structures and pore throat size distributions in 3D-printed samples from MIP experiments. This study helps better replicate natural rocks by understanding petrophysical models and behavior of 3D-printed samples through adjusting post-processing effect.

## 4 Discussion

In order to have a better idea of the similarity of heterogeneity of pore structures of synthetic samples to natural rocks, it is necessary to compare the multifractal characteristics of 3D-printed rocks with common types of natural rocks (Table 4). Common types of rocks of interest include shale, sandstone, tight carbonate and coal from the published results in recent years (Li et al. 2015; Anovitz et al. 2017; Liu and Ostadhassan 2017; Zhao et al. 2017a). Researchers used various experimental methods, including mercury injection porosimetry, scanning electron microscope, ultra-small-angle neutron scattering, and nuclear magnetic resonance, to quantify pore size distributions and analyze the heterogeneity of pore structures of various rock types (Table 4). All the samples demonstrate the same trend of  $D_0 > D_1 > D_2$ , confirming the multifractal characteristic of pore distribution. To avoid the scale of measurement that was imposed by different methods of testing, the ratio of  $D_1$  to  $D_0$  was chosen instead of a single parameter to provide the proportional variation rather than absolute ones.  $D_1/D_0$  indicates the dispersion of porosity with respect to the pore size, meaning the smaller the value, the higher the heterogeneity should be (Mendoza et al. 2010). Based on the average values from multiple samples, shale and sandstone exhibit the most largest values of  $D_1/D_0$ , whereas 3D-printed rocks have the least values (Table 4), which indicates that 3D-printed rocks have the highest heterogeneity of pore structure compared to common types of

**Table 4** Comparison of multifractal characteristics between 3D-printed rocks with common types of natural rocks from literature review

| Rock type                    | Porosity (%) | $D_0$  | $D_1$  | $D_1/D_0$ | Average $D_1/D_0$ | Experiment methods   |
|------------------------------|--------------|--------|--------|-----------|-------------------|--|
| 3D printed rocks             | 21.1980      | 0.9905 | 0.8312 | 0.8392    | 0.8244            | MIP  |
|                              | 2.0500       | 1.0332 | 0.8354 | 0.8085    |                   |  |
|                              | 0.1530       | 1.0332 | 0.8861 | 0.8576    |                   |  |
|                              | 0.6430       | 1.0332 | 0.8186 | 0.7923    |                   |  |
| Shale <sup>1</sup>           | 9.7500       | 1.7394 | 1.7149 | 0.9859    | 0.9768            | Scanning electron microscope (SEM) image analysis                  |
|                              | 10.2000      | 1.7846 | 1.7716 | 0.9927    |                   |  |
|                              | 6.7500       | 1.7243 | 1.6495 | 0.9566    |                   |  |
|                              | 6.5000       | 1.7637 | 1.6930 | 0.9599    |                   |  |
|                              | 6.3000       | 1.8496 | 1.8289 | 0.9888    |                   |  |
|                              | 9.4790       | 1.7362 | 1.6383 | 0.9436    |                   |  |
| Sandstone <sup>2</sup>       | 17.9070      | 1.7732 | 1.7271 | 0.9740    | 0.9792            | Ultra-small-angle Neutron scattering (SANS) and SEM image analysis |
|                              | 15.1980      | 1.7217 | 1.7033 | 0.9893    |                   |  |
|                              | 24.2640      | 1.7785 | 1.7708 | 0.9957    |                   |  |
|                              | 18.8750      | 1.7602 | 1.7488 | 0.9935    |                   |  |
|                              | 15.7900      | 0.8470 | 0.8330 | 0.9835    |                   |  |
|                              | 12.9000      | 0.8870 | 0.8190 | 0.9233    |                   |  |
| Tight Carbonate <sup>3</sup> | 13.6300      | 0.8360 | 0.7050 | 0.8433    | 0.9080            | Nuclear magnetic resonance (NMR) measurements                      |
|                              | 8.2600       | 0.8100 | 0.7210 | 0.8901    |                   |  |
|                              | 10.0000      | 0.8660 | 0.7790 | 0.8995    |                   |  |
|                              | 2.3600       | 1.0000 | 0.9740 | 0.9740    |                   |  |
|                              | 2.8100       | 1.0000 | 0.9640 | 0.9640    |                   |  |
|                              | 10.5300      | 1.0000 | 0.8850 | 0.8850    |                   |  |
| Coal <sup>4</sup>            | 8.7700       | 1.0000 | 0.8600 | 0.8600    | 0.9146            | MIP  |
|                              | 8.9500       | 1.0000 | 0.8900 | 0.8900    |                   |  |

The data of natural rocks come from the literature. <sup>1</sup>Bakken shale data from SEM image analysis (Liu and Ostadhassan 2017). <sup>2</sup>St. Peter Sandstone in Illinois and Michigan Basins from the result by Anovitz et al. (2017). <sup>3</sup>Permian Lucaogou Formation of Jimusaer Sag, Junggar Basin (Zhao et al. 2017a). <sup>4</sup>Coal rock from Hancheng Mine, Weibai coalfield (Li et al. 2015). Also note that samples are selected partially to be compared

natural rocks. Improving the homogeneity of pore structure of 3D-printed rocks is essential to better resemble their transport as well as geomechanical properties of natural samples.

The depth of infiltrant penetration into the 3D-printed sample affects the resulting transport and geomechanical properties. As illustrated in the method section, the penetration depth range for current samples is around 2–7 mm, whereas ideally, the infiltrant is expected to get distributed among the microstructures uniformly to better support the particles. For example in clastic rocks, clay matrix supports the particles similar to those expected from the infiltrant. The effectiveness of infiltration is determined by various factors, including the viscosity of infiltrant, duration of infiltration and connectivity of pore network in 3D-printed samples (Kunchala and Kappagantula 2018; Ishutov et al. 2018). Less viscous infiltrant can generate better penetration, whereas the geomechanical performance of 3D-printed samples is compromised. It is highly suggested to examine infiltrants with different viscosities and compare the results for the sample with the most uniform penetration and optimum strength. Capillary forces cause infiltration, which can be improved by extending the duration of samples being exposed to the infiltrant or reducing the pore throat size through more advanced printing techniques. Additionally, adjusting the particle size of the powders and binder saturation can optimize the connectivity of pore network and increase capillary forces for better penetration of infiltration. Also, vacuuming the samples helps to improve pore network by sucking in the infiltrant to penetrate deeper into the interior of the 3D-printed parts (Stumpf et al. 2018). In future studies, different techniques will be examined to provide an improved penetration of the infiltrant to further study petrophysical, geomechanical and transport properties of the samples.

## 5 Conclusion

This study characterized the petrophysical properties of the rock analogues 3D-printed in gypsum powder using MIP experiments by applying multifractal analysis. Four samples were 3D-printed using one gypsum powder and binder but different infiltrant and coating. Increasing the concentration of infiltrants resulted in them to penetrate slower into pore spaces, which generated higher porosity values, while coating process also affected the porosity and permeability to some extent. Based on PSD data from MIP experiments, 3D-printed rocks have clustered pore sized and negative skewness of pore throat distributions. The majority of pore sizes concentrate in the interval of 10–20  $\mu\text{m}$ , which belongs to the class of micropores. A small portion of pores lie in 10–20 nm, representing nanopore category. 3D-printed powder-based rocks follow the multifractal characteristics in terms of pore throat structure. Two main factors affected the heterogeneity of pore throat size distribution of 3D-printed rocks are sample orientation placement in the chamber and infiltration. 3D-printed rocks show a homogeneous structure of micropores (or seepage-pores) distribution but a heterogeneous structure in regard to the distribution of nanopores (or adsorption-pores). While infiltration mainly affected the heterogeneous distribution of adsorption-pores more than seepage-pores, 3D-printed rocks with infiltration or coating have a higher heterogeneity of pore structure compared to other common types of natural rocks based on the multifractal characteristics. This study is useful for guiding the optimal post-processing in preparing samples to substitute in petrophysical, transport and geomechanical experiments of natural rocks.

**Acknowledgements** The author greatly appreciates the American Association of Petroleum Geologists Foundation for awarding the 2017 Grand-in-aid. Co-author, Dr. Bo Liu, is supported by University Nursing Program for Young Scholars with Creative Talents in Heilongjiang Province (UNPYSCT-2015077).

## Compliance with Ethical Standards

**Conflict of interest** The Authors declare that they have no conflict of interest.

## References

- Anovitz, L.M., Freiburg, J.T., Wasbrough, M., Mildner, D.F., Littrell, K.C., Pipich, V., Ilavsky, J.: The effects of burial diagenesis on multiscale porosity in the St. Peter Sandstone: an imaging, small-angle, and ultra-small-angle neutron scattering analysis. *Mar. Pet. Geol.* **92**, 352–371 (2017)
- Bird, N., Díaz, M.C., Saa, A., Tarquis, A.M.: Fractal and multifractal analysis of pore-scale images of soil. *J. Hydrol.* **322**, 211–219 (2006)
- Brady, B.H., Brown, E.T.: *Rock mechanics: for underground mining*. Springer Science & Business Media, Berlin (2013)
- Caniego, F., Martí, M., San José, F.: Rényi dimensions of soil pore size distribution. *Geoderma* **112**, 205–216 (2003)
- Chen, Y., Joffre, D., Avitabile, P.: Underwater dynamic response at limited points expanded to full-field strain response. *J. Vib. Acoust.* **140**, 051016 (2018)
- Choi, H.-H., Kim, E.-H., Park, H.-Y., Cho, G.-H., Jung, Y.-G., Zhang, J.: Application of dual coating process and 3D printing technology in sand mold fabrication. *Surf. Coat. Technol.* **332**, 522–526 (2017)
- Clarkson, C.R., Solano, N., Bustin, R.M., Bustin, A., Chalmers, G., He, L., Melnichenko, Y.B., Radliński, A., Blach, T.P.: Pore structure characterization of North American shale gas reservoirs using USANS/SANS, gas adsorption, and mercury intrusion. *Fuel* **103**, 606–616 (2013)
- Costa, A.: Permeability-porosity relationship: A reexamination of the Kozeny–Carman equation based on a fractal pore-space geometry assumption. *Geophys. Res. Lett.* **33**, L02318 (2006)
- Daigle, H., Johnson, A., Thomas, B.: Determining fractal dimension from nuclear magnetic resonance data in rocks with internal magnetic field gradients. *Geophysics* **79**, D425–D431 (2014)
- Ding, P., Di, B., Wang, D., Wei, J., Li, X.: P and S wave anisotropy in fractured media: experimental research using synthetic samples. *J. Appl. Geophys.* **109**, 1–6 (2014)
- Dullien, F.A.: *Porous Media: Fluid Transport and Pore Structure*. Academic Press, Cambridge (2012)
- Feder, J.: *Fractals*. Springer Science & Business Media, New York (2013)
- Fereshtenejad, S., Song, J.-J.: Fundamental study on applicability of powder-based 3D printer for physical modeling in rock mechanics. *Rock Mech. Rock Eng.* **49**, 2065–2074 (2016)
- Giesche, H.: Mercury porosimetry: a general (practical) overview. *Part. Part. Syst. Charact.* **23**, 9–19 (2006)
- Giffin, S., Littke, R., Klaver, J., Urai, J.: Application of BIB–SEM technology to characterize macropore morphology in coal. *Int. J. Coal Geol.* **114**, 85–95 (2013)
- Gong, L., Fu, X., Gao, S., Zhao, P., Luo, Q., Zeng, L., Yue, W., Zhang, B., Liu, B.: Characterization and prediction of complex natural fractures in the tight conglomerate reservoirs: a fractal method. *Energies* **11**, 2311 (2018)
- Grassberger, P., Procaccia, I.: Characterization of strange attractors. *Phys. Rev. Lett.* **50**, 346 (1983)
- Guo, Z., Du, D., Liu, F., et al.: Coating process of multi-material composite sand mold 3D printing. *China Foundry*. **14**, 498–505 (2017)
- Hansen, J., Skjeltorp, A.: Fractal pore space and rock permeability implications. *Phys. Rev. B*. **38**, 2635 (1988)
- Head, D., Vanorio, T.: Effects of changes in rock microstructures on permeability: 3-D printing investigation. *Geophys. Res. Lett.* **43**, 7494–7502 (2016)
- Hodder, K.J., Nychka, J.A., Chalaturnyk, R.J.: Process limitations of 3D printing model rock. *Prog. Addit. Manuf.* **3**(3), 173–182 (2018)
- Hou, Q., Li, H., Fan, J., Ju, Y., Wang, T., Li, X., Wu, Y.: Structure and coalbed methane occurrence in tectonically deformed coals. *Sci. China Earth Sci.* **55**, 1755–1763 (2012)
- Ishutov, S., Hasiuk, F.J., Fullmer, S.M., Buono, A.S., Gray, J.N., Harding, C.: Resurrection of a reservoir sandstone from tomographic data using three-dimensional printing. *AAPG Bull.* **101**, 1425–1443 (2017)
- Ishutov, S., Hasiuk, F.J., Harding, C., Gray, J.N.: 3D printing sandstone porosity models. *Interpretation*. **3**, SX49–SX61 (2015)
- Ishutov, S., Jobe, T.D., Zhang, S., Gonzalez, M., Agar, S.M., Hasiuk, F.J., Watson, F., Geiger, S., Mackay, E., Chalaturnyk, R.: Three-dimensional printing for geoscience: fundamental research, education, and applications for the petroleum industry. *AAPG Bull.* **102**, 1–26 (2018)
- Jiang, C., Zhao, G.-F., Zhu, J., Zhao, Y.-X., Shen, L.: Investigation of dynamic crack coalescence using a gypsum-like 3D printing material. *Rock Mech. Rock Eng.* **49**, 3983–3998 (2016)

- Katz, A., Thompson, A.: Fractal sandstone pores: implications for conductivity and pore formation. *Phys. Rev. Lett.* **54**, 1325 (1985)
- Khatibi, S., Ostadhassan, M., Tuschel, D., Gentzis, T., Bubach, B., Carvajal-Ortiz, H.: Raman spectroscopy to study thermal maturity and elastic modulus of kerogen. *Int. J. Coal Geol.* **185**, 103–118 (2018)
- Knabe, R., Wang, Y., et al.: Permeability characterization on tight gas samples using pore pressure oscillation method. *Petrophysics* **52**, 437–443 (2011)
- Kong, L., Ostadhassan, M., Li, C., Tamimi, N.: Rock physics and geomechanics of 3-D printed rocks. In: ARMA-2017-0776. American Rock Mechanics Association, ARMA (2017)
- Kong, L., Ostadhassan, M., Li, C., Tamimi, N.: Can 3-D printed gypsum samples replicate natural rocks? An experimental study. *Rock Mech. Rock Eng.* (2018a). <https://doi.org/10.1007/s00603-018-1520-3>
- Kong, L., Ostadhassan, M., Li, C., Tamimi, N.: Pore characterization of 3D-printed gypsum rocks: a comprehensive approach. *J. Mater. Sci.* **53**, 5063–5078 (2018b). <https://doi.org/10.1007/s10853-017-1953-1>
- Kunchala, P., Kappagantula, K.: 3D printing high density ceramics using binder jetting with nanoparticle densifiers. *Mater. Des* (2018)
- Lai, J., Wang, G.: Fractal analysis of tight gas sandstones using high-pressure mercury intrusion techniques. *J. Nat. Gas Sci. Eng.* **24**, 185–196 (2015)
- Li, B., Liu, R., Jiang, Y.: A multiple fractal model for estimating permeability of dual-porosity media. *J. Hydrol.* **540**, 659–669 (2016a)
- Li, B.-L.: *Fractal Dimensions*. Wiley, Hoboken (2002)
- Li, C., Ostadhassan, M., Gentzis, T., Kong, L., Carvajal-Ortiz, H., Bubach, B.: Nanomechanical characterization of organic matter in the Bakken formation by microscopy-based method. *Mar. Pet. Geol.* **96**, 128–138 (2018a)
- Li, C., Ostadhassan, M., Guo, S., Gentzis, T., Kong, L.: Application of PeakForce tapping mode of atomic force microscope to characterize nanomechanical properties of organic matter of the Bakken Shale. *Fuel* **233**, 894–910 (2018b)
- Li, W., Liu, H., Song, X.: Multifractal analysis of Hg pore size distributions of tectonically deformed coals. *Int. J. Coal Geol.* **144**, 138–152 (2015)
- Li, W., Wang, C., Shi, Z., Wei, Y., Zhou, H., Deng, K.: The description of shale reservoir pore structure based on method of moments estimation. *PLoS ONE* **11**, e0151631 (2016b)
- Ling, K., He, J., Pei, P., Wang, S., Ni, X., et al.: Comparisons of Biot's coefficients of Bakken core samples measured by three methods. In: 50th US Rock Mechanics/Geomechanics Symposium. American Rock Mechanics Association (2016)
- Liu, K., Ostadhassan, M.: Quantification of the microstructures of Bakken shale reservoirs using multi-fractal and lacunarity analysis. *J. Nat. Gas Sci. Eng.* **39**, 62–71 (2017)
- Liu, K., Ostadhassan, M., Kong, L.: Fractal and Multifractal Characteristics of Pore Throats in the Bakken Shale. *Transp. Porous Media* 1–20 (2018)
- Liu, K., Ostadhassan, M., Kong, L., et al.: Pore structure heterogeneity in middle Bakken formation. In: 51st US Rock Mechanics/Geomechanics Symposium. American Rock Mechanics Association (2017)
- Lopes, R., Betrouni, N.: Fractal and multifractal analysis: a review. *Med. Image Anal.* **13**, 634–649 (2009)
- Loucks, R.G., Reed, R.M., Ruppel, S.C., Hammes, U.: Spectrum of pore types and networks in mudrocks and a descriptive classification for matrix-related mudrock pores. *AAPG Bull.* **96**, 1071–1098 (2012)
- Malik, S., Smith, L., Sharman, J., Holt, E.M., Rigby, S.P.: Pore structural characterization of fuel cell layers using integrated mercury porosimetry and computerized X-ray tomography. *Ind. Eng. Chem. Res.* **55**, 10850–10859 (2016)
- Mandelbrot, B.B.: *The Fractal Geometry of Nature*. WH Freeman, New York (1983)
- Martínez, F.S.J., Martín, M., Caniego, F., Tuller, M., Guber, A., Pachepsky, Y., García-Gutiérrez, C.: Multifractal analysis of discretized X-ray CT images for the characterization of soil macropore structures. *Geoderma* **156**, 32–42 (2010)
- Mendoza, F., Verboven, P., Ho, Q.T., Kerckhofs, G., Wevers, M., Nicolai, B.: Multifractal properties of pore-size distribution in apple tissue using X-ray imaging. *J. Food Eng.* **99**, 206–215 (2010)
- Muller, J.: Characterization of pore space in chalk by multifractal analysis. *J. Hydrol.* **187**, 215–222 (1996)
- Nabawy, B.S., Géraud, Y., Rochette, P., Bur, N.: Pore-throat characterization in highly porous and permeable sandstones. *AAPG Bull.* **93**, 719–739 (2009)
- Nasseri, M., Rao, K., Ramamurthy, T.: Anisotropic strength and deformational behavior of Himalayan schists. *Int. J. Rock Mech. Min. Sci.* **40**, 3–23 (2003)
- Oropallo, W., Piegł, L.A.: Ten challenges in 3D printing. *Eng. Comput.* **32**, 135–148 (2016)
- Ostadhassan, M., Liu, K., Li, C., Khatibi, S.: *Fine Scale Characterization of Shale Reservoirs: Methods and Challenges*. Springer, New York (2018)

- Ostadhassan, M., Zeng, Z., Zamiran, S., et al.: Geomechanical modeling of an anisotropic formation-Bakken case study. In: 46th US Rock Mechanics/Geomechanics Symposium. American Rock Mechanics Association (2012)
- Pittman, E.D.: Relationship of porosity and permeability to various parameters derived from mercury injection-capillary pressure curves for sandstone (1). AAPG Bull. **76**, 191–198 (1992)
- Primkulov, B., Chalaturnyk, J., Chalaturnyk, R., Zambrano Narvaez, G.: 3D Printed sandstone strength: curing of furfuryl alcohol resin-based sandstones. 3D Print. Addit. Manuf. **4**, 149–156 (2017)
- Ramamurthy, T.: Strength and modulus responses of anisotropic rocks. Compr. Rock Eng. **1**, 313–329 (1993)
- Riedi, R.H., Crouse, M.S., Ribeiro, V.J., Baraniuk, R.G.: A multifractal wavelet model with application to network traffic. IEEE Trans. Inf. Theory **45**, 992–1018 (1999)
- Saidi, F., Bernabé, Y., Reuschlé, T.: Uniaxial compression of synthetic, poorly consolidated granular rock with a bimodal grain-size distribution. Rock Mech. Rock Eng. **38**, 129–144 (2005)
- Schön, J.H.: Physical Properties of Rocks: Fundamentals and Principles of Petrophysics. Elsevier, Amsterdam (2015)
- Shen, Z., Sheng, J.J., et al.: Experimental study of asphaltene aggregation during CO<sub>2</sub> and CH<sub>4</sub> injection in shale oil reservoirs. In: SPE Improved Oil Recovery Conference. Society of Petroleum Engineers (2016)
- Squelch, A.: 3D printing rocks for geo-educational, technical, and hobbyist pursuits. Geosphere **14**, 360–366 (2018)
- Stumpf, M., Travitzky, N., Greil, P., Fey, T.: Sol-gel infiltration of complex cellular indirect 3D printed alumina. J. Eur. Ceram. Soc. **38**, 3603–3609 (2018)
- Suzuki, A., Watanabe, N., Li, K., Horne, R.N.: Fracture network created by 3-D printer and its validation using CT images. Water Resour. Res. **53**, 6330–6339 (2017)
- Taha, I., Abdellatif, M., Dietz, P.: Infiltration and coating of rapid prototyping parts. Adv. Eng. Mater. **7**, 91–96 (2005)
- Tian, W., Han, N.: Preliminary research on mechanical properties of 3D printed rock structures. Geotech. Test. J. **40**, 483–493 (2017)
- Tien, Y.M., Tsao, P.F.: Preparation and mechanical properties of artificial transversely isotropic rock. Int. J. Rock Mech. Min. Sci. **37**, 1001–1012 (2000)
- Tillotson, P., Sothcott, J., Best, A.I., Chapman, M., Li, X.-Y.: Experimental verification of the fracture density and shear-wave splitting relationship using synthetic silica cemented sandstones with a controlled fracture geometry. Geophys. Prospect. **60**, 516–525 (2012)
- Vázquez, E.V., Ferreira, J.P., Miranda, J., González, A.P.: Multifractal analysis of pore size distributions as affected by simulated rainfall. Vadose Zone J. **7**, 500–511 (2008)
- Vogler, D., Walsh, S.D., Bayer, P., Amann, F.: Comparison of surface properties in natural and artificially generated fractures in a crystalline rock. Rock Mech. Rock Eng. **50**, 2891–2909 (2017)
- Wang, H., Rabieci, M., Lei, G., Wang, S., et al.: A novel granular profile control agent for steam flooding: synthesis and evaluation. In: SPE Western Regional Meeting. Society of Petroleum Engineers (2017)
- Wang, L., Fu, Y., Li, J., Sima, L., Wu, Q., Jin, W., Wang, T.: Mineral and pore structure characteristics of gas shale in Longmaxi formation: a case study of Jiaoshiba gas field in the southern Sichuan Basin. China. Arab. J. Geosci. **9**, 733 (2016)
- Wang, L., Zhao, N., Sima, L., Meng, F., Guo, Y.: Pore structure characterization of the tight reservoir: a systematic integration of mercury injection and nuclear magnetic resonance. Energy Fuels **32**, 7471–7484 (2018a)
- Wang, X., Hou, J., Song, S., Wang, D., Gong, L., Ma, K., Liu, Y., Li, Y., Yan, L.: Combining pressure-controlled porosimetry and rate-controlled porosimetry to investigate the fractal characteristics of full-range pores in tight oil reservoirs. J. Pet. Sci. Eng. **171**, 353–361 (2018b)
- Wang, Z.: Seismic anisotropy in sedimentary rocks, part 2: laboratory data. Geophysics **67**, 1423–1440 (2002a)
- Wang, Z.: Seismic anisotropy in sedimentary rocks, part 1: a single-plug laboratory method. Geophysics **67**, 1415–1422 (2002b)
- Wardlaw, N.C., Taylor, R.: Mercury capillary pressure curves and the interpretation of pore structure and capillary behaviour in reservoir rocks. Bull. Can. Pet. Geol. **24**, 225–262 (1976)
- Webb, P.A.: An introduction to the physical characterization of materials by mercury intrusion porosimetry with emphasis on reduction and presentation of experimental data. Micromeritics Instrum, Corp Norcross Ga (2001)
- Wong, P., Howard, J., Lin, J.-S.: Surface roughening and the fractal nature of rocks. Phys. Rev. Lett. **57**, 637 (1986)
- Xiong, F., Jiang, Z., Li, P., Wang, X., Bi, H., Li, Y., Wang, Z., Amooie, M.A., Soltanian, M.R., Moortgat, J.: Pore structure of transitional shales in the Ordos Basin, NW China: effects of composition on gas storage capacity. Fuel **206**, 504–515 (2017)

- Zhang, Y., Lebedev, M., Al-Yaseri, A., Yu, H., Xu, X., Sarmadivaleh, M., Barifcani, A., Iglauer, S.: Nanoscale rock mechanical property changes in heterogeneous coal after water adsorption. *Fuel* **218**, 23–32 (2018)
- Zhao, P., Wang, Z., Sun, Z., Cai, J., Wang, L.: Investigation on the pore structure and multifractal characteristics of tight oil reservoirs using NMR measurements: permian Lucaogou Formation in Jimusaer Sag, Junggar Basin. *Mar. Pet. Geol.* **86**, 1067–1081 (2017a)
- Zhao, Y., Zhu, G., Dong, Y., Danesh, N.N., Chen, Z., Zhang, T.: Comparison of low-field NMR and microfocus X-ray computed tomography in fractal characterization of pores in artificial cores. *Fuel* **210**, 217–226 (2017b)
- Zhou, S., Liu, D., Cai, Y., Yao, Y.: Fractal characterization of pore–fracture in low-rank coals using a low-field NMR relaxation method. *Fuel* **181**, 218–226 (2016)

## Affiliations

Lingyun Kong<sup>1</sup>  · Mehdi Ostadhassan<sup>1</sup> · Bo Liu<sup>2</sup> · Chunxiao Li<sup>1,3</sup> · Kouqi Liu<sup>1</sup>

<sup>1</sup> Department of Petroleum Engineering, University of North Dakota, Grand Forks, ND, USA

<sup>2</sup> Accumulation and Development of Unconventional Oil and Gas, State Key Laboratory Cultivation Base Jointly-constructed By Heilongjiang Province and Ministry of Science and Technology, Northeast Petroleum University, Daqing, China

<sup>3</sup> Harold Hamm School of Geology and Geological Engineering, University of North Dakota, Grand Forks, ND, USA